History of Medicine, 2023, 9(1): 1110–1126
DOI: 10.17720/2409-5834.v9.1.2023.132

The Synthesis of Adjuvanted Iron Oxide Nanoparticles with RGD and TNF

Husam Ahmad Mahmood Al-Zohyri[1*], Mohd Basyaruddin Bin Abdulrahman[2]

1 Department of Chemistry, University Putra Malaysia, Serdang-43400, Selangor, Malaysia
EM: husambt@yahoo.com
2 Department of Chemistry, University Putra Malaysia, Serdang-43400, Selangor, Malaysia

*Corresponding author: Husam Ahmad Mahmood Al-Zohyri (husambt@yahoo.com)

Received: 20 January 2023 **Accepted:** 15 April 2023

Citation: Zohyri HAMA, Abdulrahman MBB (2023) The Synthesis of Adjuvanted Iron Oxide Nanoparticles with RGD and TNF. History of Medicine 9(1): 1110–1126. https://doi.org/10.17720/2409-5834.v9.1.2023.132

Abstract

Cancer had become the modern age disease and took over AIDS in the 80s & lung cancer occupies over half of the infected patients. Tumour necrosis factor (TNF) is potentially lethal to cancer cells and normal cells in a non-selective manner. To mitigate the non-selective action of the TNF on healthy tissues, it is vital to develop targeted nano-delivery systems capable of regulating optimum doses selectively to cancer cells and minimizing untoward toxicity to normal tissues. Here comes (RGD) homing peptides sequencing (Arg-Gly-Asp) attached to a courier molecule IONP, The IONP was synthesized from chemical co-precipitation of iron salts and scaffold with PEG coating. Its physicochemical properties, cytotoxicity, and potential as contrast agents were then evaluated. IONP at 10 nm size was synthesized at 60 minutes and 800 rpm stirring time. The coated IONP showed excellent aqueous dispensability and good negative contrast with a transverse relaxation rate of 9.85 mM-1S-1. The homing peptides and TNF attachment were achieved after coating IONP with PEG to act as a scaffold and further decrease cytotoxicity. The whole system was characterized and systematically interpreted as a function of newly formed functional groups, particle size, surface structure, surface topography, surface area, and surface charge. The system was responsive to an acidic environment and controlled the TNF dissolution released rate. The system also induced obvious cytotoxicity and apoptosis post-48 h treatment. The apoptosis study verified the ability of the system to intensify the apoptotic population in A549 while minimizing cell death in MRC5. The system reflects a potential outstanding treatment efficacy demonstrated selective cytotoxicity towards A549 than MRC5. It is believed that IONP-System attached with RGD holds great selective targeting and enhances the optimum chemotherapeutic dosage for human lung cancer with less unwarranted toxicity to normal human lung fibroblast.

Keywords
IONP, RGD, TNF, Cancer

On a worldwide scale of cancer, lung cancer is the leading death cause among all other cancers. It is estimated that more than 1.5 million patients perish from cancer annually. According to an annual analysis of cancer types and related deaths, lung cancer is gradually becoming the biggest shareholder of all other cancers over the decades (Hanspeter, 2001). The survival rate after five years of diagnosis for lung cancer patients is the least of all cancer at less than 20%, which strongly indicates the ineffectiveness of treatment and its minimal efficacy. On the other hand, this highlight's an extreme need for a more effective treatment solution (Burris, 2009). The current treatment option for lung cancer is chemotherapy. Most treatment varieties are orally administrated and very few are

---

intravenous. However, current treatments exert severe systemic side effects because of non-specificity and non-localized delivery to targeted tissues (Tseng et al., 2008). Targeting lung tissues would be an elegant solution to maximize the efficacy of lung cancer treatment.

Inhalation as a delivery route would be a good choice of treatment hence the localization of administered drug. Inhalation route of administration offers several advantages over routes when it comes to the localized treatment of cancer, mainly minimized side effects. This is a result of localized therapy plus the ability to deliver high doses besides having higher compliance of patients due to its ease. The lung's internal surface area is as much as 130-180 m^2 which gives an advantage of hyper absorption of drugs (Weibel., 2009). Homing peptides are becoming more frequently related to cancer topics regarding theranostics (Eisaku et al., 2021). iRGD is a 9-amino acid cyclic tumour-homing peptide (sequence: CRGDKGPDC) while RGD poses the same form but unlike it's predesesor; not ciclical. Since iRGD is not a drug that can affect cancer cells, TNF (an immunogenic cytotoxin very effective against cancer cells) which have a thousand-fold less cytotoxicity when coupled with RGD/iRGD; however, RGD/iRGD has a shallow penetration to tissues, thus the need for iron oxide nanoparticle for this purpose (Teesalu T et al., 2009). This 3-component system has specificity, penetration and effectiveness against cancer cells (Houdong et al., 2011). The choice of iron oxide nanoparticle as a core particle is of necessity due to its deep tissue penetration and relatively very low cytotoxicity (Hernбndez et al., 2020).

Materials and methods

IONP synthesis

The thermal decomposition method for iron oxide nanoparticles was used to get it as hydrophilic as possible for later stages. The thermal decomposition method for iron oxide nanoparticles requires iron salts ferric trichloride ($FeCl_3$) and ferrous chloride ($FeCl_2$) dissolved in 150ml distilled water in the presence of nitrogen gas to prevent oxidation at 800 rpm and 45°C for 10min. Later, 20ml of NH_3 was added to the mixture, and the temperature was brought up to 80°C while the reaction was kept running for 50min. After turning off the temperature and stirring, the mixture was allowed to cool, and a strong neodymium magnet was used to collect the iron oxide nanoparticles from the solution. Next, the liquid part was discarded, and the resulting mixture was washed with acetone, stirred, and drained three times. Finally, the washed mixture was ready to be transferred to an oven set at 80°C for 24hrs. The solid iron oxide mixture can then be ground gently and thoroughly to make a fine powder form for analysis and complete building of the system. This experimental procedure was modified from (Mahdavi et al., 2013).

Iron oxide facile PEGylation

PEGylation was facially derived from coating with polyethene glycol (PEG). PEG 10,000 Da (PEG10,000) was used to coat powdered IONP as a physical coating, which requires powdered IONP to be dissolved in distilled water and PEG10,000 was added at a rate of 5%. This experiment dissolved 3.0 g iron oxide nanoparticles in 100 ml distilled water, and 0.15g PEG 10,000 was added to the mixture. The process should be at room temperature at a stirring speed of 500 rpm for 24 hrs. After 24 hrs, the mixture was centrifuged at 10,000 rpm for 30 min, and the sediment was collected and dried in the oven at 50°C for 24 hrs (Mun et al., 2016).

RGD attachment

Since PEG is described as a good scaffolding and coating material, the next step in building up the complete system, physical attachment can be achieved here. Three concentrations of RGD were used here to create three variant concentrations which were 0.5%, 0.75% and 1% w/w to the PEGylated IONP. For a batch of 3.0 g of PEGylated iron oxide weighted 0.015 g, 0.02 g and 0.03 g were used, respectively, and dissolved in distilled water at room temperature with a stirring speed of 500 rpm for 24 hrs. Later, the sediment was collected by subjecting the mixture to centrifugation at a rate of 10.000 RPM for 30mins. Finally, the mixture was dried in the oven at 45°C for 24 hrs (Mun et al., 2016).

TNF attachment

The final step in completing the system is to add TNF as its drug since the PEG surface area could hold more molecules; the above method is also implied here. A 24-hr run time at room temperature with a 450 rpm stirring rate. After 24hrs, the sediment was collected via centrifugation for 30 min at 10,000 rpm and then transferred to an oven set at 45˚C for 24 hrs (Mun et al., 2016).

Results and Discussion

In this study, the scaffold of iron oxide nanoparticle (PEG-IONP) was functionalized with the Arg- Gly-Asp homing peptide ligand (RGD) or cyclic RGD (iRGD) to ensure its ability to actively and autonomously target tumour cells. Both RGD and iRGD peptides are binding ligands that can bind and act with the integrins receptors αVβ3, which are overexpressed on tumoral endothelial (Damjanovich et al., 1992; Danhier et al., 2012; Ding et al., 2015; Bianconi et al., 2016; Babu et al., 2017). In addition, iRGD peptides are capable of homing the neurolipin-1 (NRP-1), which is also upregulated in tumoral endothelial. Suppose the RGD/iRGD-attached PEG-IONP are carrying a chemotherapeutic agent. In that case, the nanoparticle can dock on the cell's surface to deliver the agents being carried. As a proof-of-concept, PEG-IONP carrying the chemotherapeutic agent, tumour necrosis factor (TNF), and finally surface-functionalized with RGD or iRGD peptides were synthesized to determine the ability of this nanoparticle to induce apoptosis of tumour cells as a result of actively and selectively delivered TNF. Developed nanoparticles' permeability and potential toxicity were assessed using the novel co-culture technique, consortia (Figure 1).

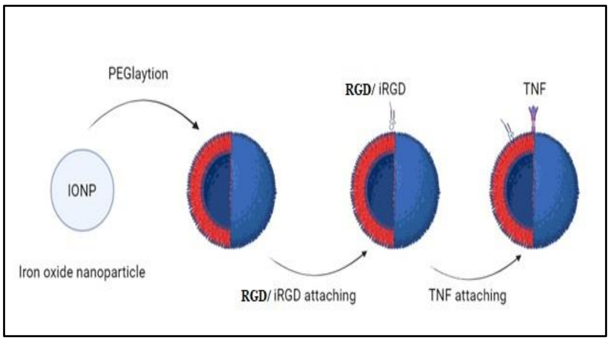

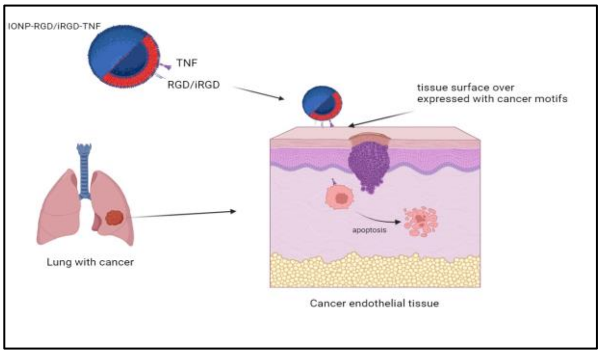

Figure 1 Synthetic scheme for the nanoparticles and the complete system's mechanism of action.

Physicochemical characterizations of Naked IONP and the system

The optimized synthesis reaction of iron oxide nanoparticle (IONP) was compaired to the standard literature database of the same molecule and as shown below (Figure 2)

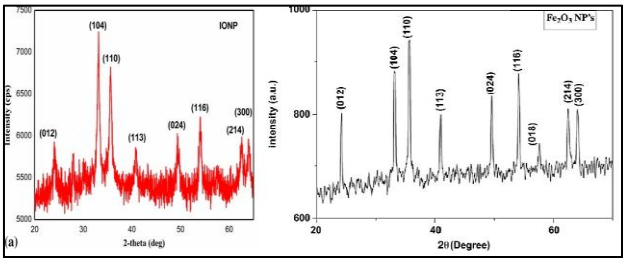

Figure 2 Synthesized IONP in comparison to the simulated pattern

Synthesised IONP demonstrate XRD patterns in good agreement compared to the simulated data. The main eight sharp peaks observed at $2\theta = 24$, 33, 36, 41, 49.5, 54, 61.5 and 63 correspond to (012), (104), (110), (113), (024), (116), (214) and (300) (Mishra et al., 2015). In addition, tiny and very low-intensity peaks might be related to the instrumental error or the presence of trace amounts of impurities.

The optimized synthetic reaction for creating the nanoparticles (IONP), the chemotherapeutic agent attached to nanoparticles (PEG-IONP), and the nanoparticles with homing peptides whose surfaces were scaffolded with PEG then RGD and iRGD homing peptide ligands attached (TNF-RGD-PEG-IONP) were found to be essentially the same with the synthesis of all four nanoparticles following a straightforward, one-pot solvothermal reaction procedure. Figure 3 shows nanoparticle suspensions were produced after the reaction procedure. Separately, the dark suspensions were produced when TNF was attached to IONP, and in vivo simulation by co-culture consortia studies to assess the effectiveness. Once each nanoparticle system was isolated, washed and dried, powder X-ray diffraction (PXRD) analysis was performed (Figure 3).

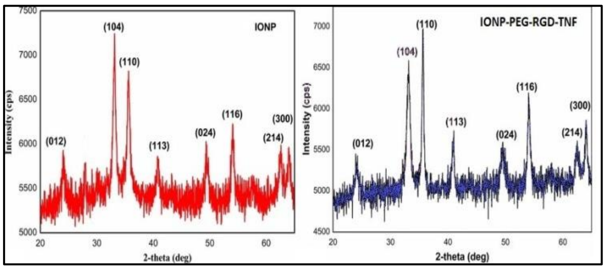

Figure 3 Powder X-ray diffraction (PXRD) patterns for IONP (red) and IONP-PEG-RGD-TNF (blue).

The structural identification of all nanoparticles in powder form was assessed using powder X-ray diffraction analysis (PXRD). As shown in Figure 4.3, the experimental diffraction patterns for IONP were observed to be coincident with the theoretical diffraction pattern simulated from the single structure of IONP. The characteristic diffraction pattern of IONP at 2θ = 13.2°, 33.4°, 36.7°, 41.7°, 49.4°, 53.0°, 62.1°, 66.5°, 71.7° and 79.6°, which corresponded to planes of (011), (002), (112), (022), (013), (222), (114), (233), (134) and (044) (Mishra et al., 2015a). It is important to note that the obtained diffraction peaks of IONP and IONP-PEG-RGD-TNF were well retained after the attachment of TNF and functionalization process of RGD. Therefore, this PXRD analysis provided several critical findings, which are loading of TNF on IONP did not disrupt the symmetry of the IONP structure, the structure of IONP was robust enough to enough to withstand the conditions needed to functionalize its surface with RGD, and bulk phase purity of all four nanoparticles was proven.

Functional group analysis

Successful surface functionalization of IONP-PEG by RGD and iRGD was first confirmed by Fourier transform infrared spectroscopy measurement (FTIR) (Figure 2). The parent IONP FTIR spectrum exhibited several characteristic absorption bands that serve as a baseline for comparison with RGD attached to IONP: The FTIR spectrum of synthesized IONP displayed three strong bands around 3383.42, 1634.15 and 480.69 cm^{-1} (Figure 6B). Kumar and Singhal reported the presence of similar bands at 472, 1634 and 3438 cm^{-1} when colloidal β-Fe_2O_3 was synthesized in the presence of varying Co^{2+} amounts. Based on our study, the vibration bands could be 529.92 cm^{-1} (Fe), 1634.15 cm^{-1} (H_2O bending vibration) and a broad peak at 3383.42 cm^{-1}. The presence of organic molecules on the surface of IONP has been reported to influence the FTIR peaks, and the broad peak was observed around 529.92 cm−1 instead of two sharp peaks, which might be due to the PEG on the surface of IONP. The weak band at 3837.93 cm^{-1} could be attributed to the PEG's unsaturated nitrogen (C-N) compounds. The close-up FTIR spectrum (Figure 4.2) upon functionalization of the surface of IONP with the RGD homing peptides shows considerable differences when compared with the parent IONP spectrum. It is essential first to note that all those absorption bands observed in the FTIR spectrum for the parent IONP remain present in the FTIR spectra for IONP-PEG-RGD.

Secondly, several characteristic absorption bands of RGD emerge as follows: (i) 3300-3100 cm-1 corresponds to overlapping amide A and B absorption bands; (ii) 1736 cm^{-1} strongly indicates the presence of a new carbonyl $v_{C=O}$ stretching frequency that is formed upon protonation of the carboxylic acid groups from RGD peptide (Psarra et al., 2017); (iii) 1648 cm^{-1} is assigned to amide I; (iv) 1577 cm^{-1} exhibits a slight increase in absorbance due to an overlap of $v_{C=N}$ between the 2-methylimidazolate of PEG and the Arg residue of RGD; (v) 1375 cm^{-1} is ascribed to a v_{C-N} stretching frequency originating from RGD; and (vi) 524 cm^{-1} is attributed to the $v_{C=O}$ bending frequency from amide VI. This might be due to the possibility that the Arginine residue of RGD acts as a Lewis base while interacting with coordinatively unsaturated PEG sites at the surface of the IONP (Rцder et al., 2017). These assignments for the FTIR spectra provide strong evidence for chemical bond formation between RGD to the IONP-PEG.

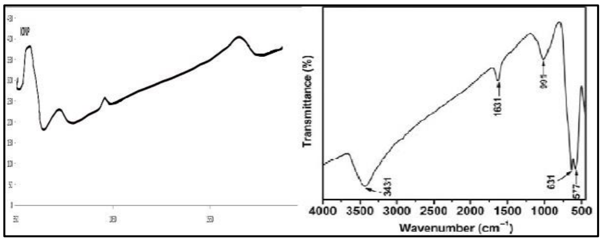

Figure 4 Fourier transform-infrared spectroscopy (FTIR) spectra comparing synthesized IONP and simulated IONP.

Synthesised IONP demonstrate FTIR patterns in good agreement compared to the simulated data. The main five peaks observed at 3431, 1631, 991, 631 and 577 Cm^{-1} are aligned together.

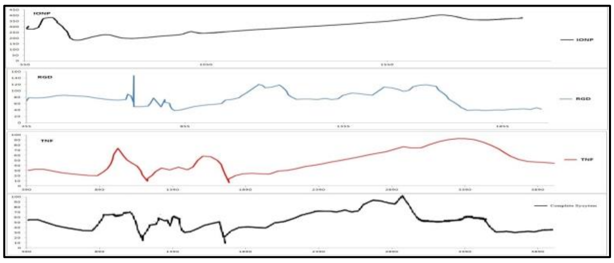

Figure 5 Fourier transform-infrared spectroscopy (FTIR) spectra comparing IONP (Black), RGD (Blue), TNF (Red) and Complete system (2nd Black)

RAMAN spectroscopy was also conducted to identify certain bonds that refer to the presence of IONP-system components. The measured Raman spectra of these groups are presented in the following to constitute the difficulty of differentiating these groups via spontaneous Raman scattering, especially under natural conditions in solution. Hence, to get an idea of the Raman shifts and intensity ratios of promising Raman labels such as alkyne, azide or deuterated moieties, Raman spectra of solvents and Raman-labeled groups are compared with their untagged counterparts. In addition, the measured spectra also serve as the basis for simulations used to estimate the detection limit and test the performance of quantitative analysis techniques.

All peptides and polymers mainly consist of carbon, oxygen and hydrogen atoms. Accordingly, they all show Raman bands in similar regions depending on the different vibrational modes. The most important types of vibrations and Raman shift regions are listed in table 4.1. C=O vibrations only exist in acetylated group molecules. O-H vibrations are covered by water.

Table 1 Characteristic vibrations in Raman spectra.

Type of vibration	Region of Raman shift
C-C Vibration	800 cm^{-1} -122 cm^{-1}
C-H stretching	2800 cm^{-1} - 3100 cm^{-1}
C-H deformation	1380 cm^{-1} – 1470 cm^{-1}
C-OH stretching	1100 cm^{-1} – 1210 cm^{-1}
C-OH deformation	750 cm^{-1} -800 cm^{-1}
C=O stretching	1550 cm^{-1} -1800 cm^{-1}
O-H stretching	3200 cm^{-1} -3800 cm^{-1}
O-H deformation	1600 cm^{-1} – 1700 cm^{-1}

Table 1 displays the structure of the most relevant occurring groups. The corresponding normalized Raman spectra in the solid phase and solution at 1M concentration show the signifying broadening, intensity, and spectral shifts of individual peaks caused by the solvation in water. In particular, the characteristic PEG peaks in the solid phase at 1032 cm^{-1} and 1280 cm^{-1} are not observable in solution, and PEG is nearly indistinguishable from IONP. Only the homing peptides could be identified in the mixture by the strong peak at 920 cm^{-1}.

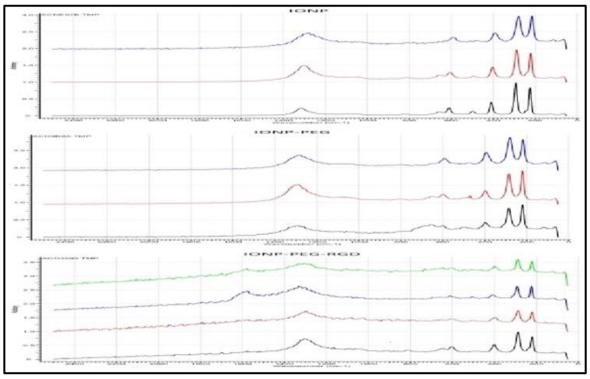

Figure 6 RAMAN Raman spectra of IONP, IONP-PEG and IONP-PEG-RGD

Similar circumstances can be recognized in the normalized Raman spectra of polymers and peptides, which are building blocks for the IONP system. The Raman spectra show strongly overlapping peaks varying in intensity, especially between RGD and iRGD. Compared to regular groups, the main difference is the high intensity detected in the C-H stretch region (2800 cm^{-1} – 3100 cm^{-1}) caused by the CH3 moiety. The strong C=O stretching vibration can also be observed for all acetylated groups at H1642 cm^{-1}. This Raman band contributes to the so-called amide 1 region (1640 cm^{-1}–1700 cm^{-1}) of peptides and is convoluted with various other compounds (P. LAGANT et al., 1984, N. K. Howell et al., 1999).

Particle size and structural morphology analysis

A Field emission scanning electron microscopy (FE-SEM) identified particle size and structural morphology. Accordingly, Field emission scanning electron microscopy (FE-SEM) images revealed that all particle sizes were within the nanoscale size regime (100-

500 nm) for drug delivery (Rizvi & Saleh, 2018) (Figure 4.4). This is an important finding, given that nanoscale particles are needed to promote uptake and cytotoxicity within cancer cells (Foroozandeh & Aziz, 2018). The smaller-sized particles, which is commonly < 6 μm depending on certain factors such as cell variation and culture environment (Gustafson et al., 2015), can reduce phagocytosis by alveolar macrophages and thereby increase their retention rate within epithelial cells (Oberdцrster et al., 2005; Ahmad et al., 2012). The nonsurface functionalized IONP, IONP-PEG-RGD-TNF and IONP-PEG-iRGD-TNF's average size was 8.1 ± 0.15 and 12.2 ± 1.3 nm, respectively. The grinding process could explain the different sizes and uniformities of IONP during the nanoparticle fine powdering preparation.

The nanoparticles were synthesised at various stirring rates and were spherical particles with little to no aggregation (Figure 4.4). Stirring during reaction has been thought to promote homogeneous dispersion of reaction medium and to minimise particle aggregation during synthesis. However, low turbulence in the reaction medium induced by slow agitation may cause inhomogeneous dispersion of particles, thus limiting particle aggregation to form larger particles. This can be observed in Figure 4.4, where broader size distribution (depicted by a higher dispersity index in Table 4.1) was observed for samples stirred at lower rates (600 rpm) than samples at 800 rpm. More uniform particle size was observed at the stirring rate of 600 rpm, but the particle size decreased as the stirring rate increased from 1000 rpm.

Based on the reports from similar studies, further increase of stirring rates to higher than 800 rpm in this work may produce smaller particles (Ibarra-Sбnchez et al., 2013; Rahmawati et al., 2017). Rahmawati et al. (2017) found that increasing the stirring rate from 500 to 700 rpm to synthesise magnetite using the coprecipitation-ultrasonic irradiation method produced similar spherical particles. Still, the particle size decreased as the stirring rate increased. When a stirring rate higher than 800 rpm was used, the particles started to form large aggregates. Ibarra-Sбnchez et al. (2013) obtained IONP of different sizes and saturation magnetisation by increasing the stirring rates in the thermal decomposition of iron (III) acetylacetonate. They observed that particle size initially increased from 7.7 nm at 0 rpm to 10.5 nm at 100 rpm, then decreased to 7.8 nm when the stirring rates were higher than 100 rpm.

The cause of different sizes produced by different stirring rates is the difference in mass transport rates in the colloidal system during synthesis. At lower stirring rates, particle growth is governed mainly by the diffusion of nuclei due to limited mass transfer in the solution. As a result, more time is required to form particles of uniform size. Hence higher dispersity was observed at 600 rpm. Increasing the stirring rates to the optimal setting (in this case at 800 rpm) promotes better mass transfer and, consequently, better control of particle growth. This is because diffusion of nuclei and convection phenomenon (motion of reaction medium) is in balance, leading to narrow size distribution. However, convection dominates as mass transport rates increase when the stirring rate exceeds the optimal rate. As a result, convection favours nucleation and limits particle growth, reducing particle size. Therefore, a smaller mean particle size was observed for 800 rpm (8.1 ± 0.5 nm) compared to 600 rpm (11.4 ± 0.5 nm), as shown in Table 2.

Table 2 Particle diameter, particle dispersity and saturation magnetisation of IONP synthesised at four different stirring rates.

Stirring rate (rpm)	Particle diameter (nm)
600	11.4 ± 0.5 (d = 0.17)
800	8.1 ± 0.5 (d = 0.06)
10000	7.6 ± 0.8 (d = 0.09)

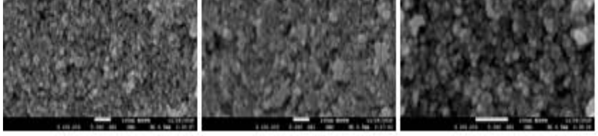

Figure 4.7 FE-SEM images of IONP samples synthesised with different stirring rates at 100KX magnification

Vibrating sample magnetometer (VSM) results in Figure 4.8 and Table 4.2 show a saturation magnetisation (Ms) value of 47.7 emu/g for

IONP stirred at 800 rpm, similar to the value reported by Belaпd et al. (2018).

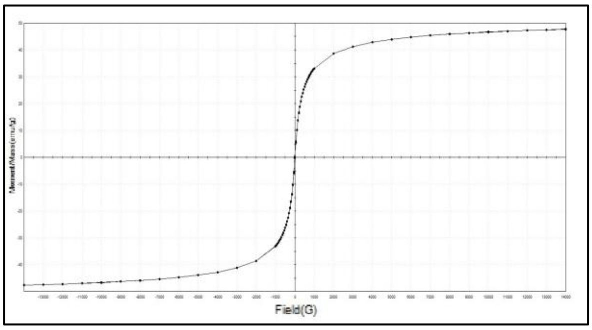

Figure 8 Field-dependent hysteresis loops (M–H) at room temperature for IONP obtained 800rpm stirring rates

The synthesis procedure of monodisperse IONP with a particle size of approximately 10 nm was successfully optimised by varying the stirring rate and ageing time. An earlier report by Yu et al. (2004) used grounded Fe(O)OH as the precursor for the IONP synthesis. Still, this work has shown that monodisperse nanoparticles could also be obtained without reducing the precursor to smaller particles before synthesis.

4.5 Surface topography analysis

To further investigate the topography or surface character, atomic force microscopy measurements (AFM) was performed in tapping mode measurement (Figure 4.6). Three-dimensional images showed apparent differences in the surface characters of IONP, IONP-PEG-iRGD and IONP-PEG-RGD/iRGD-TNF. A quantitative parameter for the average roughness of each surface, Ra, was employed to assess these differences. The R_a value measures the peaks and valleys found on sample surfaces. For IONP and IONP-PEG, smaller peaks and valleys resulted in R_a values of 8.1 and 10.9 nm, respectively. On the other hand, a pattern of moderate peaks and valleys was observed for the surface character of IONP-PEG-RGD-TNF and IONP-PEG-iRGD-TNF, resulting in a higher R_a value of 12.2 and 12.6 nm, respectively.

The results of these measurements imply that the surface functionalization of IONP and iRGD does increase the surface roughness of the nanoparticles, which strongly correlates with the FE-SEM images obtained (Figure 4.7). Indeed, these observations are significant findings as the rougher surface character of nanoparticles is typically correlated with a higher potential for influencing the internalization of lung cancer cells (Muthukumar et al., 2014). Furthermore, these findings were supported by Niu and co-workers when enhanced cellular uptake was observed after being treated with rough modified silica nanoparticles compared to smooth nanoparticles (Niu et al., 2015).

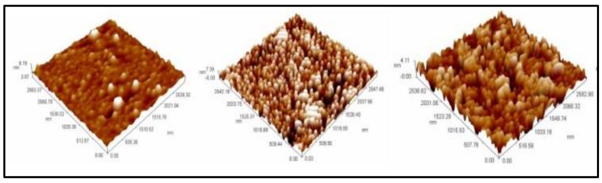

Figure 9 Atomic force microscope images

Surface charge and hydrodynamic size

The hydrodynamic size and surface charge were obtained by dynamic light scattering (DLS), frequently employed due to its non-destructive method of determining particle size in suspensions (Hirschle et al., 2016). The average hydrodynamic sizes of IONP and IONP-PEG were similar, with values of 79 ± 4.5 and 114 ± 3.0 nm, respectively (Figure 4.10). However, upon attachment with RGD and iRGD, the hydrodynamic size increased to 140 ± 5 and 205 ± 5 nm, respectively. It is noted that hydrodynamic size, as measured by dynamic light scattering techniques, typically leads to higher values than those observed in FE-SEM measurements because the hydration layer around the nanoparticles is included within the calculated size (Eaton et al., 2017). Therefore, increasing hydrodynamic size correlates with the trend observed for the FE-SEM measurements (Figure 4.7). Concerning the development of nanoparticles for cancer applications, particle size signifies a vital role in the therapeutic process, including uptake and immune response (Carvalho et al., 2018). For example, the nanoparticles are designed more than normal vessels diameter and can accommodate a leaky tumour typically between 40-200 nm in size (Sarin et al., 2009). Next, the zeta potential was utilized to confirm that the RGD and iRGD were separately attached to the IONP surface after the scaffolding and functionalization process. Concerning the surface charge of the nanoparticles, the zeta potential for IONP was slightly less positive than IONP-PEG (+4.5 to +4.9, respectively). Interestingly, both IONP and IONP-PEG were significantly less positive when compared with IONP-PEG-RGD (+5.06) and IONP-PEG-iRGD (+5.06). This is another critical trend to observe as the more positively charged the surface of nanoparticles is, the more likely they are to be taken up by cancer cell membranes and remain within the cell for extended periods (Blanco et al., 2015). The surface charge is crucial to increasing the interaction with the targeting tumour membrane (Ramos et al., 2017).

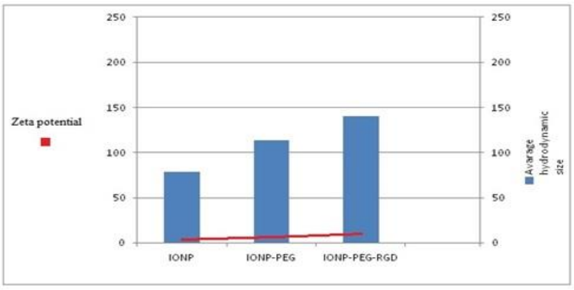

Figure 10 Average hydrodynamic size (blue) and zeta potential (red)

Thermal study for physical state analysis

Mass loss was compared using thermal gravimetric analysis (TGA) under continuous N2 flow. The comparative TGA of IONP, IONP-PEG and IONP-PEG-iRGD-TNF are shown in Figure 11. Likewise, TGA depicts a trend of IONP-PEG-RGD-TNF < IONP-PEG < IONP with respect to thermal stability. The nanoparticles with PEG, including IONP-PEG-RGD-TNF and IONP-PEG, begin to thermally decompose over the 450 °C range correspondingly parent IONP is thermally stable up to at least 375 °C. The initial decomposition temperature of PEG is 375 °C (Sung-ku Kwon et al., 2014). The initial decomposition of IONP and IONP-PEG probably starts with the loss of structural integrity, resulting in the loss of structures commencing at about 375 °C. The next decomposition was shown in IONP-PEG-RGD-TNF due to the IONP decomposition. This phenomenon of more thermally stable systems compared to its core molecule; gives insight into the presence of RGD peptides and TNF attached to the system, consistent with the other physicochemical properties mentioned in earlier sections. The findings corroborate the previously reported IONP coupled with homing peptides, and TNF demonstrated early mass loss compared with naked IONP (Sung-ku Kwon et al., 2014). In pharmaceuticals, TGA is explored to evaluate solid-state kinetics, such as the decomposition of drugs in various drug formulations. Moreover, TGA is applied in the drug quality control process, including accelerated stability which is conducted for a minimum of 6 months to ensure the end product meets the required specification (ICH Q1A, 2003).

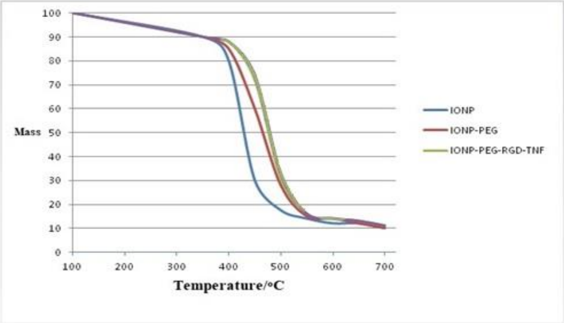

Figure 11 Thermal gravimetric analysis (TGA) under N2 flow

Drug loading efficacy

Figure 4.12 presents the TNF Loading efficiency (%) of IONP-PEG-RGD/iRGD. The equation of the TNF standard curve in ethanol was (y = 1290.6x + 2374, R2 = 0.999) (Appendix A). The highest obtained DL% was 8.19% ± 0.52% and 55.08% ± 1.68% with 750 µg of TNF. Furthermore, DL% was inversely reduced with increasing the TNF weight up to 1000 µg, which can be explained as the maximum capacity of the nanomolecular at 750 µg. It's concluded that scaffolded IONP can hold approximately 19.7% of drug-release studies and later for in-vitro studies. The drug loading and efficiency values are considered acceptable compared to the literature for optimal activities in treating cancer tissue (F. Mozar & Chowdhury, 2015).

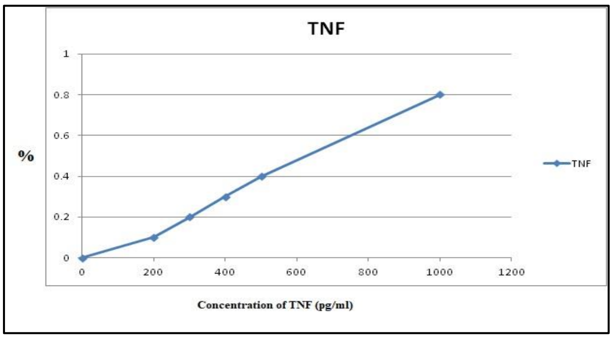

Figure 12 Tumor necrosis alpha (TNF-α) standard curve.

In vitro drug release simulation

The drug release profile of IONP-PEG-RGD was assessed using a dialysis bag method. The concentration of TNF diffused through a dialysis membrane into the release media consists of a fixed volume of simulated lung fluid (SLF), and 0.5% Tween 80 was determined within a 48-hour release duration. Pulmonary surfactant in biological lung fluid was absent in the SLF used in this work. Thus, Tween 80 was added into the release media to increase TNF solubility and promote the diffusion of TNF through the membrane. The release was conducted in two different pH; one study was in pH 7.4 to simulate the neutral pH in the body system, and the other was carried out in a more acidic environment (pH 6.0) to simulate the condition around cancerous cells. Drug release of TNF from both IONP-PEG-RGD was studied under the same conditions to compare their release profiles. Both formulations demonstrated a lower release in the simulated extracellular environment of normal tissue (SLF, pH 7.4) than in the simulated intracellular tumour environment in SLF at, pH 6.0, as seen in Figure 4.10. This pattern agrees with other literary publications, suggesting an accelerated release under acidic conditions for lipid-based formulation (Asmawi et al., 2019). Approximately 41% TNF was released from both IONP-PEG-RGD in SLF pH 7.4 within a 48-hour period, which is higher compared to IONP-PEG-RGD/iRGD-TNF (< 21% release). In the acidic environment (pH 6.0), IONP-PEG-RGD rapid release was exhibited during the initial 6 hours, with more than 41% release detected in the release media. Then, a gradual release to 80% was observed until 48 hours.

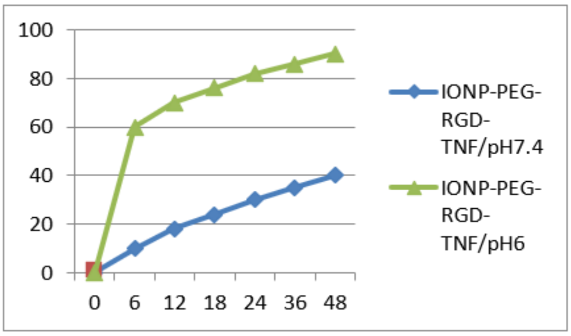

Figure 13 Drug release profiles of IONP-PEG-RGD using dialysis membrane in SLF at two different pH

Magnetic Resonance Imaging of IONP

Phantom experiments to evaluate the imaging properties of IONP were performed using a 3 T MRI scanner. Only transverse relaxation times (T_2) and T_2-weighted images were acquired. No significant positive contrast was seen for longitudinal relaxation times (T_1) within the concentration range of 0 to 0.5 mg/mL prepared for the experiment. A higher concentration of IONP was not tested because the nanoparticles exhibited in vitro cytotoxicity on MRC5 at 0.5 mg/mL and in apoptosis experiments.

Clear negative contrast was observed on T_2-weighted images presented in Figure 4.14, beginning from the concentration of 0.5 mg/mL IONP. The measured relaxation rate was plotted against the concentrations of IONP (Figure 4.11). Transverse relaxation rate (R_2) increased linearly with the increasing concentrations of IONP, similar to other findings published in the literature (Alipour et al., 2018; R. Wei et al., 2018 ;S6nchez-Cabezas et al., 2019). Relaxivity, r_2, was calculated at 9.85 $mM^{-1}s^{-1}$, determined from the linear fit of the data according to equation 3.5.

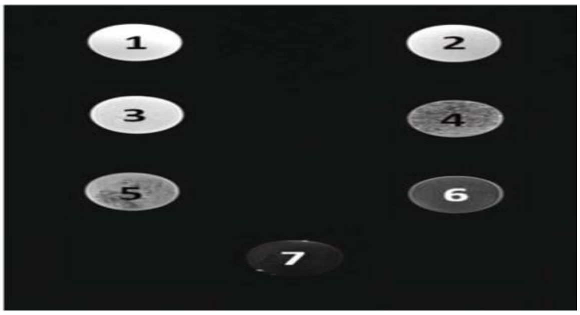

Figure 13 T2-weighted images of IONP-PEG

The value of r_2 in this work is similar to the 11 nm silica-coated spherical IONP measured at the same magnetic field strength (3 T) (Alipour et al., 2018). The results could be attributed to the effect of particle aggregation after PEGylation. Previous FE-SEM images of IONP coated with PEG (Figure 7) revealed the presence of monodisperse particles. However, particle aggregation was seen after scaffolding with PEG (Figure 7). Although the core size of the IONP remains unchanged, particles agglomeration has caused a larger hydrodynamic size, resulting in more considerable local field inhomogeneity that affects its transverse relaxivity (Joos et al., 2017;

Ta et al., 2017). In addition, the relaxivity was measured by embedding the IONP in 1% agarose gel. According to Joos, this process could cause agglomeration and may distort the relaxation rates (Joos et al., 2017).

Surface coating of the IONP is crucial to improve the biocompatibility of IONP and to maintain colloidal stability. Its surface chemistry will determine the relaxation rates and contrast of the MRI images. Modifying the surface chemistry to tune the proton relaxation will enable higher contrast and transverse relaxivity (LaConte et al., 2007). IONP-PEG displayed good negative contrast, but positive contrast could not be observed within the tested concentration range (0 to 0.5 mg/mL). PEG scaffolding may hinder direct interactions between the iron oxide core and the protons, resulting in invisible positive contrast.

In contrast, PEG coating shortened T_2 relaxation rates and produced good negative contrast. The results presented in this work are limited to the IONP-PEG only, but varying the coating thickness by using a different molecular weight of polyethyleneglycol coating on IONP surface was reported in the previous studies to affect longitudinal as well as transverse relaxivity (LaConte et al., 2007; Hajesmaeelzadeh et al., 2016). Furthermore, both studies reported that the r_2 decreased as coating thickness increased. Therefore, a relaxivity comparison of IONP-PEG with different weight ratios may prove helpful in selecting the optimal amount of PEG as IONP coating.

Although these results are currently limited to transverse relaxation rates, further improvements to the method may be modified to measure longitudinal relaxation. Modifying concentration range and measurement parameters might ensure adequate representation of IONP-PEG as an efficient contrast agent.

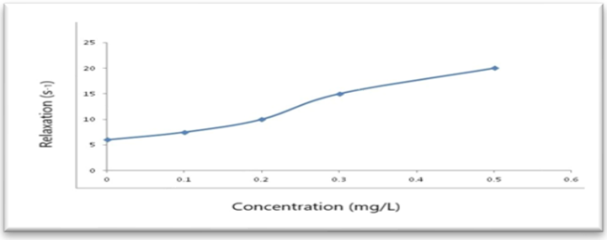

Figure 15 Relaxation rate of IONP-PEG as a function of concentration in mg/mL to determine relaxivity, r2, of IONP-PEG

In vitro cytotoxicity of IONP and the complete system

In vitro cytotoxicity of IONP and IONP-PEG-RGD-TNF was carried out on normal human lung fibroblast cells (MRC5) and adenocarcinoma human alveolar basal epithelial cells (A549). The cytotoxicity of IONP and IONP-PEG-RGD was determined by the percentage of cell viability using XTT assay after treatment for 24, 48 and 72 hours. IONP exhibits a cytotoxic effect if cell viability is less than 60%, whereas it is non-toxic if it is more than 80% (International Organization for Standardization [ISO], 2009).

As shown in Figure 16, cell viability decreased dose-dependent for both MRC5 and A549. The trend is consistent with previous in vitro cytotoxicity studies of IONP, with or without surface coating on other cell types, such as rat liver cells (BRL 3A) (Thorat et al., 2016), J774 (murine macrophage cells) (Naqvi et al., 2010), human bronchial (16HBE) and alveolar epithelial cells (A549) (Guadagnini et al., 2015).

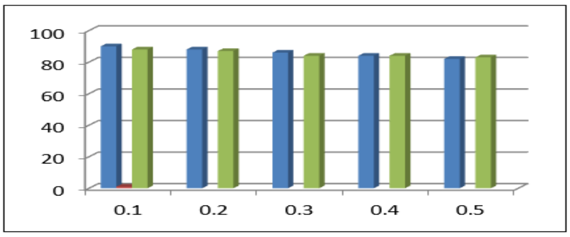

24hrs incubation

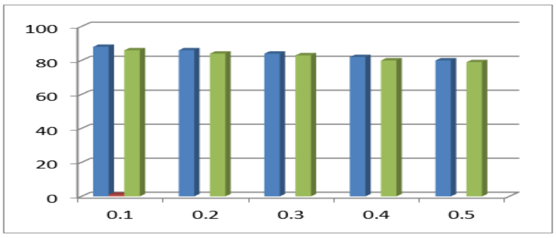

48hrs incubation

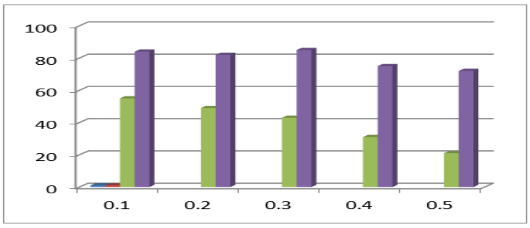

72hrs incubation

Figure 16 Percentage of cell viability of MRC5 and A549 analysed by XTT assay after treatments with IONP and IONP-PEG-RGD-TNF at five different concentrations

Regardless of incubation time, >80% MRC5 cell viability was observed after exposure to IONP, IONP-PEG-RGD-TNF at the concentration range of 0.1-0.5 µg/ mL but slight toxicity (<80% cell viability) was found on MRC5 above 0.3 µg/ mL, which agrees well with previous studies on in vitro cytotoxicity of IONP (Dadfar et al., 2019). However, less concentration of IONP and IONP-PEG-RGD/iRGD-TNF was needed to exhibit a similar cytotoxic effect on A549 after 24 hours of exposure; over 80% of cells were viable when exposed to 0.1 µg/ mL IONP, while only 80% viability was recorded at the highest concentration tested (0.5 µg/ mL). In comparison, only 57% of A549 cells were viable after 24 hours of exposure to 0.5 µg/ mL IONP-PEG-RGD-TNF (Dwivedi et al., 2014).

After 24 hours of exposure, cell death on A549 at the highest concentration tested (0.5 µg/ mL) was significant compared to MRC5 ($p<0.05$). Prolonging the exposure time to 48 and 72 hours increased the growth inhibition of A549 significantly, but no significant difference was observed in MRC5 viability. At 72 hours of exposure, the difference in viability between MRC5 and A549 was significantly above the concentration of 0.1 µg/ mL ($p<0.0001$). These results showed that the cytotoxicity of IONP and IONP-PEG-RGD-TNF on A549 increased with increasing concentration of IONP and IONP-PEG-RGD-TNF increased exposure duration.

Half maximal inhibitory concentrations (IC_{50}) for MRC5 and A549 for all three incubation times are tabulated in Table 4.3. A lower concentration of IONP and IONP-PEG-RGD-TNF was generally required to induce 50% of cell death on A549 than MRC5. These results demonstrated that IONP and IONP-PEG-RGD-TNF have higher in vitro cytotoxicity to A549 than normal lung fibroblast cells (MRC5).

Table 3 IC50 values of IONP and IONP-PEG-RGD-TNF on MRC5 and A549 at 24H. 48H and 72H

Time (h)	IONP IC_{50} (ng/ml)		IONP-PEG-RGD-TNF IC_{50} (ng/ml)	
	MRC5	A549	MRC5	A549
24	23.8	22.4	28.7	40.8
48	21.6	20.7	27.4	38.5
72	11.2	2.9	13.9	5.1

Cell death mechanism induced by IONP and IONP-PEG-RGD-TNF may be caused by oxidative stress and loss of membrane integrity, leading to apoptosis of A549 (M. I. Khan et al., 2012; Dwivedi et al., 2014; Das et al., 2020). Cell exposure to a higher concentration of IONP was reported to elevate the level of peroxidation stress and reduce antioxidant enzyme activity, possibly due to intracellular reactive oxygen species (ROS) generation (Dwivedi et al., 2014). Fenton or Fenton-like reactions and Haber-Weiss reactions that produce free radicals (O_2-, OH-) and hydrogen peroxide (H_2O_2) may contribute to ROS generation by IONP, resulting in cellular damage (e.g. loss of membrane integrity) and subsequently initiate programmed cell death (Paunovic et al., 2020). Interestingly, Khan et al. (2012) did not observe a similar cytotoxic effect on normal lung fibroblast cells. However, further research may be needed to confirm the cytotoxicity and proapoptotic effects of IONP and IONP-PEG-RGD-TNF in non-malignant cells.

The IONP-PEG-RGD-TNF is potentially safe to be used as a diagnostic agent on healthy individuals and cancer patients. No cytotoxicity was exhibited on MRC5 up to the 0.5 µg/ mL concentration. In contrast, only 40 µg/mL IONP was needed to reduce the viability of HepG2 cells below 80% (Mohammadi et al., 2021), while a significant decrease in Saccharomyces cerevisiae cell viability was observed at the concentration of 50 µg/mL (Asif et al., 2020). Growth inhibition of IONP and IONP-PEG-RGD-TNF on MRC5 and A549 increased as the concentration increased to 0.5 µg/ mL, and the exposure time was prolonged to 72 hours. However, cellular uptake and toxicity of IONP depend not only on the size, morphology and surface coating of the nanoparticles but also on the cell types (Mahmoudi et al., 2011).

Apoptosis assay induced by nanoparticles

Given that IONP and IONP-PEG-RGD-TNF were selective in enhancing the cytotoxicity of cancer cells, the apoptotic cell populations were then quantified via flow cytometry (Figure 17). The flow cytometry measurements exposed both A549 and MRC5 cell lines to TNF, IONP and IONP-PEG-

RGD-TNF for 48h. Viable cells are depicted in the lower-left quadrant (Q1). Early apoptotic cells, which were positively stained only for Annexin V/FITC, are plotted in the lower right quadrant (Q2). Late apoptotic cells stained positive for Annexin V/FITC, and PI are plotted in the upper right quadrant (Q3). Finally, the PI-only stained necrotic cells are displayed in the upper left quadrant (Q4).

When exposed to IONP and IONP-PEG-RGD-TNF, the total percentage of apoptotic cells (Q2 + Q3) in A549 was higher than in MRC5. Furthermore, the total apoptotic cells observed after treatment with TNF alone were comparable in both A549 and MRC5 cell lines. Notably, the treatment of A549 by IONP-PEG-iRGD-TNF yielded the highest apoptotic cells (71.9%), followed by IONP-PEG-RGD-TNF (63.5%), whereas the IONP and TNF alone were 53.7% and 89% (highly toxic on its own), respectively. Furthermore, the nanoparticles IONP-PEG-RGD-TNF; 52.4% also showed fewer apoptotic cells in MRC5 than treatment by TNF alone (77.5%). These findings mean that IONP-PEG-RGD-TNF can induce apoptosis in A549 while reducing cell death in MRC5 cells. For both nanoparticles, this was attributed to the fact that the RGD homing peptides are more likely to actively bind the over-expression of αVβ3 integrins on the outer surface of A549 cells (Nieberler et al., 2017). Additionally, the fact that IONP-PEG-RGD-TNF has a six-fold lower apoptotic percentage (13.1%) in MRC5 when compared to TNF (77.5%) is evidence that IONP-PEG-RGD-TNF exhibits good safety to healthy cells. However, simultaneously, ramp up the apoptosis activity in the cancerous cells. This is ascribed to an excellent selectivity behaviour, deep internalization of CendR to NRP-1, and pH-responsive of IONP itself towards A549 cells. This is supported by a previous report that combined RGD and TNF enhanced the apoptotic in the A549 xenograft model by reducing the tumour volume and growth compared to TNF alone (Zhang et al., 2015).

Later, the investigations were translated into in vivo simulations known as Consortia to evaluate the selectivity and penetration produced by IONP-PEG-RGD-TNF towards co-cultured MRC5 and A549 cell lines.

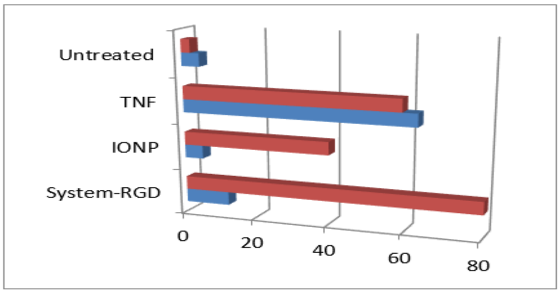

Figure 17 Quantification of apoptotic cell population obtained by flow cytometry analysis at 48 h time treated with the appropriate IC50 value (50% inhibiting concentration) of TNF, IONP, IONP-PEG-RGD-TNF

lyophilisation and cryoprotectant Selection

Lyophilisation is one of the recommended methods to enhance nanoparticle stability for long-term storage. Cryoprotectant is often added before lyophilisation to prevent molecule degradation due to the stress during the freeze-drying process, to minimise particle aggregation and to improve the dispersibility of the lyophilised nanoparticles after freeze-drying (Varshosaz et al., 2012; Almalik et al., 2017). Carbohydrates such as sucrose, mannose, trehalose and maltodextrin are easily vitrified and changed into a glassy state during freeze-drying. Thus they are preferred as a cryoprotectant (Varshosaz et al., 2012).

The freeze-thaw approach can be used in the screening process to select the optimal cryoprotectant concentration for the lyophilisation of the IONP system. This work dissolved sucrose in different percentages (10%, 12.5% and 15% w/v) in the suspension before the freeze-thaw study. The particle size of the IONP system before and after the freeze-thaw study was measured to observe any changes in particle size. All samples exhibited minimal changes in particle size and higher polydispersity index, independent of the sucrose concentration as tabulated in Table 4.4, with acceptable particle growth shown by the calculated Sf /Si ratio of less than 1.3 (Date et al., 2010).

Table 4 Particle size and PdI of the IONP after adding sucrose as cryoprotectant according to the percentage added into the formulation

Sucrose % (w/v)	Particle size (nm)	PdI	S_f/S_i ratio
0	114	0.58	n/a
10	123.1	0.67	1.08
15	127.7	0.65	1.08
20	136.8	0.64	1.2

Minimal particle size increase after adding sucrose as a cryoprotectant in various percentages agrees with the results previously reported by Varshosaz et al. (2012) and Almalik et al. (2017). In comparing several carbohydrates as a cryoprotectant, slow cooling with sucrose as a cryoprotectant at -20 °C before lyophilisation resulted in less particle growth than a fast-freezing rate at -70 °C (Varshosaz et al., 2012). Moreover, sucrose's high hygroscopicity helped shield the IONP system from mechanical stress due to ice formation surrounding the nanoparticles during freezing. The sugar will attract and hold water molecules from damaging the nanoparticles (M. K. Lee et al., 2009; Rampino et al., 2013). During freezing, the IONP system is now embedded in amorphous glasses formed by sucrose above its glass transition temperature (60 °C). Thus particle destabilisation can be prevented, and the size distribution can be preserved. However, an increased PdI value indicates higher particle aggregation after adding sucrose. This may be improved by optimising the concentration of the sucrose added as a cryoprotectant in the IONP-system suspension as demonstrated by previous studies (Ball et al., 2016; Almalik et al., 2017).

in vivo simulation by co-culture Consortia

Consortia for IONP-System was carried out on normal human lung fibroblast cells (MRC5) and adenocarcinoma human alveolar basal epithelial cells (A549). First, the affinity of the IONP-system (iRGD was only tested because of a different affinity toward the A549 cell line) was determined by absorbance after confluency was reached. Then IONP-system was introduced to the culture for 24, 48 and 72 hours. As illustrated in Figures 4.18 and 4.19.

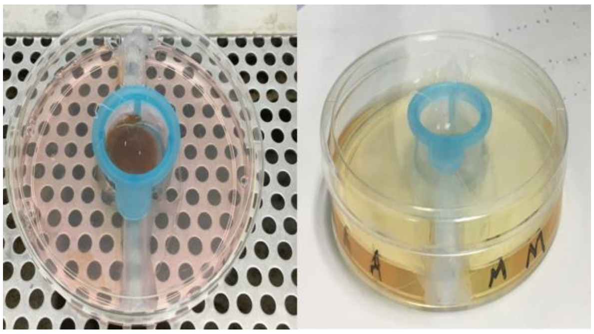

Figure 18 Consortia illustration

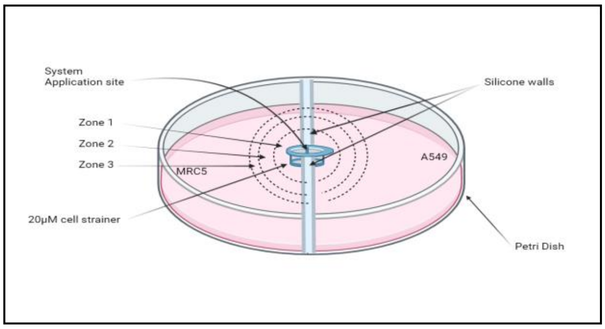

Figure 19 Consortia Zones illustration

As shown in Figure 19, around the cell strainer, the Petri- Dish was marked to represent 3 different circular zones; each is bigger than 1cm than the other, and those zones represent the penetration depth of the simulation of a tissue. The IONP-system dose used here was the same as IC_{50}; the absorbance was recorded of each zone at 24, 48 and 72 hrs, as shown in Figures 20 and 21

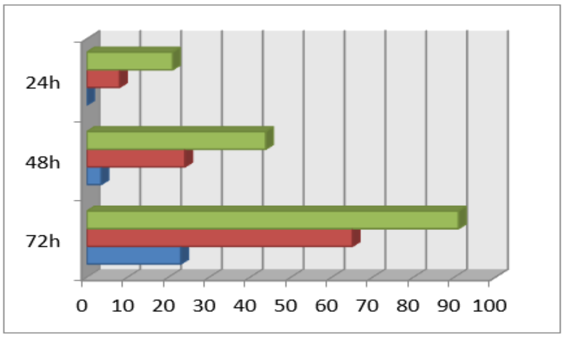

Figure 20 Consortia zone absorbance, showing separate penetration on the side of the A549 cell line; green represents the closest zone to the cell strainer, red represents the middle zone, and blue represents the outer zone

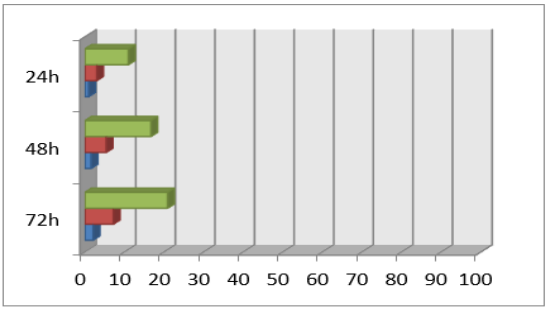

Figure 21 Consortia zone absorbance, showing separate penetration on the side of the MRC5 cell line

The first comparison between both sides of the consortia is the amount of spreading of the IONP-system to the A549 side significantly over the MRC5 side due to the high affinity of RGD towards integrins receptors αvβ3 and αvβ5 presented on A549, and that agrees with previous studies (Sugahara et al., 2015), the dispersed amount of IONP-system on the MRC5 side may be due to concentration differences and equilibrium (Rivas G, Minton AP, 2017). Thus, the simulation setting proved that the IONP system has a high affinity and selectivity toward the A549 cell line.

The second comparison is the penetration of all three zones on the A549 side; it's almost doubling every 24h, and by 72 h, the migrated amount of IONP-system is at its highest based on the proposed high affinity of αvβ3 and αvβ5 receptors, and that also agrees with previous studies (Sugahara et al., 2015). So this proves that IONP-system has a deep tissue penetration potential.

The conclusion that combines the previous findings is that IONP systems have a high affinity toward the A549 cell line and a deep tissue penetration capability.

5 conclusions

The present study investigates the potential of developing active-targeted nanoparticles RGD or iRGD-targeted (IONP) nanoparticles to increase the selectivity of the chemotherapeutic agent (TNF) towards cancer cells by exploiting the tumour microenvironment and ligand-receptor interactions. Through a straightforward synthesis and active groups attachment, this study has reported the desired loading and subsequent attachment of (IONP) with a chemotherapeutic agent (TNF) and two autonomous homing systems (RGD and iRGD), respectively.

Two synthesis parameters of IONP from chemical co-precipitation from $FeCl_2$ and $FeCl_3$, i.e. stirring rate and time, were optimised to achieve an average particle size of approximately 10 nm. As a result, spherical monodisperse IONP having saturation magnetisation of 47.7 emu/g was synthesised at 800 rpm and 60 minutes stirring time. In addition, the PEG scaffolding of the IONP was set at 5% w/w for further attachments.

Physicochemical characterisation of the IONP-System showed that the particles were spherical with a mean particle size of approximately 10 nm after, as shown by FE-SEM. In vitro, drug release studies in SLF media demonstrate higher release in the simulated cancerous environment (acidic condition) than in the neutral pH of the healthy tissues. In the SLF with a pH of 6.5, initial burst release during the first 6 hours was observed, followed by sustained release up to 48 hours. The kinetic release was found to fit the first-order kinetic model.

The IONP was very well dispersed in buffer solution and cell culture media. MRI studies using MRI phantoms suggested that IONP is potentially useful as a negative contrast agent, with its transverse relaxivity, r_2, determined at 9.85 $mM^{-1}S^{-1}$. The IONP-System exhibited dose-dependent cytotoxicity on both MRC5 and A549. The cytotoxic effect of the IONP-System was observed to be more significant on A549 than MRC5 at prolonged exposure to 72 hours, measured by the cell viability percentage of both cells. The IONP-System was

The IONP was lyophilised using sucrose as the cryoprotectant for longer storage stability. Storage stability assessment of the lyophilised formulation was conducted at room or cooler temperatures (2-8 °C). Changes in the nano size of IONP stored in a cooler environment indicated better storage stability at room temperature than in a cooler environment.

This study demonstrates that the developed magnetic nanostructure loaded with TNF and RGD/iRGD can potentially be a diagnostic and therapeutic agent in lung cancer treatment. Furthermore, monitoring of therapeutic efficacy in the tumour may be accomplished using MRI, and reduced toxicity of the formulation on MRC5 showed a promising diagnostic tool alternative, also proven via the Consortia test.

References

Alipour Z, Kheirabadi GR, Kazemi A, Fooladi M. The most important risk factors affecting mental health during pregnancy: a systematic review. East Mediterr Health J. 2018 Jul 29;24(6):549-559. doi: 10.26719/2018.24.6.549. PMID: 30079950.

Asif S, Mudassar A, Shahzad TZ, Raouf M, Pervaiz T. Frequency of depression, anxiety and stress among university students. Pak J Med Sci. 2020 Jul-Aug;36(5):971-976. doi: 10.12669/pjms.36.5.1873. PMID: 32704273; PMCID: PMC7372668.

Ball JE, Griffiths P, Rafferty AM, Lindqvist R, Murrells T, Tishelman C. A cross-sectional study of 'care left undone' on nursing shifts in hospitals. J Adv Nurs. 2016 Sep;72(9):2086-97. doi: 10.1111/jan.12976. Epub 2016 Apr 20. PMID: 27095463.

H. A. Burris, “Shortcomings of Current Therapies for Non-Small-Cell Lung Cancer: Unmet Medical Needs,” Oncogene, Vol. 28, No. 1 (Supplement), 2009, pp. S4-13. doi:10.1038/onc.2009.196

Carvalho, Josй. (2021). Carvalho 2018. 10.13140/RG.2.2.35055.87201.

Pieri C, Moroni F, Recchioni R, Marcheselli F, Falasca M, Antonicelli R, Damjanovich S. Aging impairs membrane potential responsiveness as well as opening of voltage and ligand gated Na+ channels in human lymphocytes. Arch Gerontol Geriatr. 1992 Mar-Apr;14(2):145-54. doi: 10.1016/0167-4943(92)90049-a. PMID: 15374399.

Dwivedi M, Backers H, Harishchandra RK, Galla HJ. Biophysical investigations of the structure and function of the tear fluid lipid layer and the effect of ectoine. Part A: natural meibomian lipid films. Biochim Biophys Acta. 2014 Oct;1838(10):2708-15. doi: 10.1016/j.bbamem.2014.05.011. Epub 2014 May 17. PMID: 24841755.

Eaton NR, Thompson RG Jr, Hasin DS. Eaton et al. Respond. Am J Public Health. 2015 Dec;105(12):e1-2. doi: 10.2105/AJPH.2015.302906. Epub 2015 Oct 15. PMID: 26469665; PMCID: PMC4638251.

Foroozandeh P, Aziz AA. Insight into Cellular Uptake and Intracellular Trafficking of Nanoparticles. Nanoscale Res Lett. 2018 Oct 25;13(1):339. doi: 10.1186/s11671-018-2728-6. PMID: 30361809; PMCID: PMC6202307.

Guadagnini R, Halamoda Kenzaoui B, Walker L, Pojana G, Magdolenova Z, Bilanicova D, Saunders M, Juillerat-Jeanneret L, Marcomini A, Huk A, Dusinska M, Fjellsbш LM, Marano F, Boland S. Toxicity screenings of nanomaterials: challenges due to interference with assay processes and components of classic in vitro tests. Nanotoxicology. 2015 May;9 Suppl 1:13-24. doi: 10.3109/17435390.2013.829590. PMID: 23889211.

Gustafson JL, Neklesa TK, Cox CS, Roth AG, Buckley DL, Tae HS, Sundberg TB, Stagg DB, Hines J, McDonnell DP, Norris JD, Crews CM. Small-Molecule-Mediated Degradation of the Androgen Receptor through Hydrophobic Tagging. Angew Chem Int Ed Engl. 2015 Aug 10;54(33):9659-62. doi: 10.1002/anie.201503720. Epub 2015 Jun 17. PMID: 26083457; PMCID: PMC4547777.

Hanspeter Witschi, A Short History of Lung Cancer, Toxicological Sciences, Volume 64, Issue 1, November 2001, Pages 4–6.

Contreras M, Pacheco I, Alberdi P, Dнaz-Sбnchez S, Artigas-Jerуnimo S, Mateos-Hernбndez L, Villar M, Cabezas-Cruz A, de la Fuente J. Allergic Reactions and Immunity in Response to Tick Salivary Biogenic Substances and Red Meat Consumption in the Zebrafish Model. Front Cell Infect Microbiol. 2020 Mar 10;10:78. doi: 10.3389/fcimb.2020.00078. PMID: 32211341; PMCID: PMC7075944.

Deshpande G, LaConte S, Peltier S, Hu X. Integrated local correlation: a new measure of local coherence in fMRI data. Hum Brain Mapp. 2009 Jan;30(1):13-23. doi: 10.1002/hbm.20482. PMID: 17979117; PMCID: PMC6870773.

Dwivedi M, Backers H, Harishchandra RK, Galla HJ. Biophysical investigations of the structure and function of the tear fluid lipid layer and the effect of ectoine. Part A: natural meibomian lipid films. Biochim Biophys Acta. 2014 Oct;1838(10):2708-15. doi: 10.1016/j.bbamem.2014.05.011. Epub 2014 May 17. PMID: 24841755.

Rampino A, Borgogna M, Blasi P, Bellich B, Cesaro A. Chitosan nanoparticles: preparation, size evolution and stability. Int J Pharm. 2013 Oct 15;455(1-2):219-28. doi: 10.1016/j.ijpharm.2013.07.034. Epub 2013 Jul 22. PMID: 23886649.

Mahdavi SS, Spadinger IT, Salcudean SE, Kozlowski P, Chang SD, Ng T, Lobo J, Nir G, Moradi H, Peacock M, Morris WJ. Focal application of low-dose-rate brachytherapy for prostate cancer: a pilot study. J Contemp Brachytherapy. 2017 Jun;9(3):197-208. doi: 10.5114/jcb.2017.68424. Epub 2017 Jun 13. PMID: 28725242; PMCID: PMC5509985.

Mishra VR, Sreenivasan KR, Zhuang X, Yang Z, Cordes D, Banks SJ, Bernick C. Understanding white matter structural connectivity differences between cognitively impaired and nonimpaired active professional fighters. Hum Brain Mapp. 2019 Dec 1;40(17):5108-5122. doi: 10.1002/hbm.24761. Epub 2019 Aug 12. PMID: 31403734; PMCID: PMC6865667.

Mohammadi K, Yaribash S, Sani MA, Talasaz AH. Efficacy and Safety of the Fixed-Dose Versus Variable-Dose of 4-PCC for Vitamin K Antagonist Reversal: A Comprehensive Systematic Review and Meta-Analysis. Cardiovasc Drugs Ther. 2022 Jun;36(3):533-546. doi: 10.1007/s10557-021-07192-0. Epub 2021 Apr 17. PMID: 33864534.

Muthukumar AK, Stork T, Freeman MR. Activity-dependent regulation of astrocyte GAT levels during synaptogenesis. Nat Neurosci. 2014 Oct;17(10):1340-50. doi: 10.1038/nn.3791. Epub 2014 Aug 24. PMID: 25151265; PMCID: PMC4176984.

Naqvi NH, Bechara A. The insula and drug addiction: an interoceptive view of pleasure, urges, and decision-making. Brain Struct Funct. 2010 Jun;214(5-6):435-50. doi: 10.1007/s00429-010-0268-7. Epub 2010 May 29. PMID: 20512364; PMCID: PMC3698865.

Nieberler M, Reuning U, Reichart F, Notni J, Wester HJ, Schwaiger M, Weinmьller M, Rдder A, Steiger K, Kessler H. Exploring the Role of RGD-Recognizing Integrins in Cancer. Cancers (Basel). 2017 Sep 4;9(9):116. doi: 10.3390/cancers9090116. PMID: 28869579; PMCID: PMC5615331.

Hoadley KA, Yau C, Wolf DM, Cherniack AD, Tamborero D, Ng S, Leiserson MDM, Niu B, McLellan MD, Uzunangelov V, Zhang J, Kandoth C, Akbani R, Shen H, Omberg L, Chu A, Margolin AA, Van't Veer LJ, Lopez-Bigas N, Laird PW, Raphael BJ, Ding L, Robertson AG, Byers LA, Mills GB, Weinstein JN, Van Waes C, Chen Z, Collisson EA; Cancer Genome Atlas Research Network; Benz CC, Perou CM, Stuart JM. Multiplatform analysis of 12 cancer types reveals molecular classification within and across tissues of origin. Cell. 2014 Aug 14;158(4):929-944. doi: 10.1016/j.cell.2014.06.049. Epub 2014 Aug 7. PMID: 25109877; PMCID: PMC4152462.

Oberdцrster G, Oberdцrster E, Oberdцrster J. Nanotoxicology: an emerging discipline evolving from studies of ultrafine particles. Environ Health Perspect. 2005 Jul;113(7):823-39. doi: 10.1289/ehp.7339. Erratum in: Environ Health Perspect. 2010 Sep;118(9):A380. PMID: 16002369; PMCID: PMC1257642.

Vasconcelos, Vitor & Martins, Rosбrio. (2021). Ramos et al., 2018.

Rivas G, Minton AP. Toward an understanding of biochemical equilibria within living cells. Biophys Rev. 2018 Apr;10(2):241-253. doi: 10.1007/s12551-017-0347-6. Epub 2017 Dec 12. PMID: 29235084; PMCID: PMC5899707.

Rizvi SAA, Saleh AM. Applications of nanoparticle systems in drug delivery technology. Saudi Pharm J. 2018 Jan;26(1):64-70. doi: 10.1016/j.jsps.2017.10.012. Epub 2017 Oct 25. PMID: 29379334; PMCID: PMC5783816.

Sarin SK, Kumar A, Almeida JA, Chawla YK, Fan ST, Garg H, de Silva HJ, Hamid SS, Jalan R, Komolmit P, Lau GK, Liu Q, Madan K, Mohamed R, Ning Q, Rahman S, Rastogi A, Riordan SM, Sakhuja P, Samuel D, Shah S, Sharma BC, Sharma P, Takikawa Y, Thapa BR, Wai CT, Yuen MF. Acute-on-chronic liver failure: consensus recommendations of the Asian Pacific Association for the study of the liver (APASL). Hepatol Int. 2009 Mar;3(1):269-82. doi: 10.1007/s12072-008-9106-x. Epub 2008 Nov 20. PMID: 19669378; PMCID: PMC2712314.

Sugahara H, Odamaki T, Fukuda S, Kato T, Xiao JZ, Abe F, Kikuchi J, Ohno H. Probiotic Bifidobacterium longum alters gut luminal metabolism through modification of the gut microbial community. Sci Rep. 2015 Aug 28;5:13548. doi: 10.1038/srep13548. PMID: 26315217; PMCID: PMC4552000.

Teesalu T, Sugahara KN, Ruoslahti E. Tumor-penetrating peptides. Front Oncol. 2013 Aug 27;3:216. doi: 10.3389/fonc.2013.00216. PMID: 23986882; PMCID: PMC3753659.

Andalib S, Varshosaz J, Hassanzadeh F, Sadeghi H. Optimization of LDL targeted nanostructured lipid carriers of 5-FU by a full factorial design. Adv Biomed Res. 2012;1:45. doi: 10.4103/2277-9175.100147. Epub 2012 Aug 28. PMID: 23326776; PMCID: PMC3544134.

Antoinette Weibel, Katja Rost, Margit Osterloh, Pay for Performance in the Public Sector—Benefits and (Hidden) Costs, Journal of Public Administration Research and Theory, Volume 20, Issue 2, April 2010, Pages 387–412

Xin F, Yu Y, Yang ZJ, Hou LK, Mao JF, Xia L, Wang X, Cao XC. Number of negative lymph nodes as a prognostic factor for ypN0-N1 breast cancer patients undergoing neoadjuvant chemotherapy. Tumour Biol. 2016 Jun;37(6):8445-54. doi: 10.1007/s13277-015-4640-3. Epub 2016 Jan 5. PMID: 26733172.